BeBeC-2022-D02

BREAKDOWN OF PROPELLER AIRCRAFT NOISE BY APPLYING CONVENTIONAL BEAMFORMING JOINTLY WITH IMAGING USING THE ROTATING SOURCE IDENTIFIER

Bieke von den Hoff[1], Dick Simons[1], and Mirjam Snellen[1],
[1] Section Aircraft Noise and Climate Effects, Faculty of Aerospace Engineering, Delft University of Technology
Kluyverweg 1, 2629 HS, Delft, The Netherlands

Abstract

Full-scale propeller measurements are useful to study the total noise contribution of a propeller-driven aircraft, including installation effects. Full-scale measurements under operational conditions also provide an accurate validation opportunity for propeller noise prediction models. These studies are, therefore, necessary to quantify and reduce the noise annoyance of propeller-driven aircraft. For propeller aircraft, rotating sources need to be considered. In this research, propeller noise is studied for a full-scale propeller using an acoustic microphone array. The acoustic imaging techniques used are Conventional Frequency-Domain or Time-Domain Beamforming for the stationary noise sources and the ROtating Source Identifier for the rotating noise sources. By applying these two acoustic imaging methods simultaneously, in addition to filtering in the spatial and frequency domain, also filtering in the source velocity domain can be exploited. These methods were applied to an engine run-up of a Pipistrel Velis Electro, the first fully-electric certified aircraft. This electric aircraft, placed on the ground, allows for an initial study on the present noise sources and their relative contributions. Ultimately, this information can be used to separate the measured spectrum into spectra of different noise components which in turn can be used for full-scale validation and improvement of propeller noise prediction models.

1 INTRODUCTION

Recently, the first fully-electric aircraft has been certified for flight. Although the Pipistrel Velis Electro is still the only one certified [10], many companies announced the launch of an electric aircraft. These aircraft are propeller-driven, which causes significant noise annoyance which is predicted to increase with more electric aircraft in service [2, 6]. Therefore it is important to investigate and ultimately reduce the noise production of propeller-driven aircraft. Some

studies have investigated whether electric aircraft produce less noise than their piston-engine counterpart [4, 9], but more research is needed for the propeller as noise source. To the best of the authors' knowledge, this is the first noise related research on the Pipistrel Velis Electro.

To reduce the noise emissions and annoyance of propeller-driven aircraft, the noise sources need to be analysed, and their contribution reduced during the design process of a new propeller. Semi-empirical prediction models based on wind-tunnel tests do exist to assess the propeller noise emissions, but they are hardly validated. Validation is possible with noise measurements on scale models in wind-tunnels or computational fluid dynamics software, but might be more cost effective and accurate with noise measurements on existing full-scale models in operational conditions. The measurements on full-scale models however include other aircraft sources and potential interaction effects that need to be split from the propeller noise. In addition to design, validated noise models are also essential for noise prediction for operational aircraft.

The goal of this research is to identify the sources that make up the total noise during an engine run-up of the Pipistrel Velis Electro. For the test configuration considered, the sources can either be stationary or rotational. The stationary sources include engine sources, noise from cavities in the airframe, or interaction effects of the propeller wake with the airframe. The rotational sources only include the sources due to the moving propeller blades. The sources can be separated by analysing a noise measurement with Conventional Beamforming in the Time-Domain (CTDB) or Frequency-Domain (CFDB) and the ROtating Source Identifier (ROSI). This essentially allows for filtering in the spatial, velocity, and frequency domain [12]. This can then be used to compare two different propellers on the same aircraft, or by comparing the same propeller on different aircraft, as the individual sources are known. This aids in broadening the knowledge on interaction and installation effects of propellers.

This paper is structured as follows: Section 2 introduces the acoustic imaging methods used. Section 3 explains the experimental setup for the noise measurements. The results are presented and discussed in Section 5 and the paper is concluded with some recommendations in Section 6.

2 ACOUSTIC IMAGING METHODS

Acoustic imaging methods are mostly used to separate sources in the spatial domain versus the frequency domain. However, combining different source characteristics such as its speed, allows for an extra filtering dimension. In this research three acoustic imaging methods are used. First, CTDB was used for spatial source separation of stationary sources. This method is easiest to understand and forms the basis of ROSI and therefore is explained first in Section 2.1. Then CFDB is explained in Section 2.2 which was used to separate sources not only spatially but also focus on their individual frequency characteristics. Lastly, ROSI is explained in Section 2.3. ROSI was used to focus on rotating sources.

2.1 CTDB

CTDB is based on time delays for a signal arriving at different microphones [7, 12]. These differences are caused by the fact that the acoustic signal arrives earlier on the microphone closest to the source. The purpose of this method is to correct each received signal for the time delay to a potential source location, and subsequently add the delayed signals. If indeed a source

is present at the location considered, then the delayed signals exhibit constructive interference and produce a high pressure amplitude. If there is no source present, the resulting pressure amplitude is low. This method is often referred to as delay-and-sum beamforming.

A grid of potential source locations is defined at a distance z from the microphone array with the grid centre aligned with the microphone array centre. Each of these grid locations is evaluated for a potential source emitting at time t. Typically, the selected signal length for analysis is 0.1 s. For a grid point j, the time delay Δt to a certain microphone n is defined as

$$\Delta t_{j,n} = \frac{r_{j,n}}{c} \tag{1}$$

in which $r_{j,n}$ is the distance between grid point j and microphone n, while c is the speed of sound in air. The microphone specific time delay is applied to the received signals $p_n(t)$. The delayed signals of all microphones are then summed for this grid point and the resulting reconstructed pressure signal is divided by the number of microphones. Subsequently, the reconstructed pressure is squared and then averaged over the time snapshot, resulting in the effective pressure squared $\overline{p_j^2}$. The averaged contribution is expressed as an Overall Sound Pressure Level (OSPL) by

$$\mathrm{OSPL}_j = 10\log_{10}\left(\frac{\overline{p_j^2}}{p_{\mathrm{ref}}^2}\right) + 20\log_{10}(z) \tag{2}$$

where p_{ref} is the reference pressure of 20 μPa. The minimum distance z between the microphone array and the source causes attenuation of the signal through spherical spreading and hence a correction factor is taken into account.

As the delay-and-sum method is applied in the time domain, the whole frequency range is considered. The acoustic source map resulting from this method may thus present sources occurring at different frequencies.

Note that when applying stationary beamforming methods to a moving source, the acoustic image becomes polluted with a larger spread source region or a location at a distance offset from the source. For a case with only high speed rotating sources, a ring of sources becomes visible in CTDB at a lower OSPL than the rotating source. Figure 1a shows this result. This can be explained through the reconstruction of the pressure signal; very often the rotating source passes the grid point and thus the reconstructed pressure signal exhibits a peak at every blade passage and a source seems to be present. However, the rms value will be lower than the value of the blade peak as it is not always present.

2.2 CFDB

In addition to the time-domain results, this paper also presents results over certain frequency bands created with frequency-domain beamforming. The frequencies at which a source emits, might indicate the origin or mechanism of the source. The method used for this paper is based on a least-squares minimisation between a modelled pressure signal and the measured pressure signal [7, 12]. This gives an estimation of the source power A. At grid location j and frequency f, A is determined by

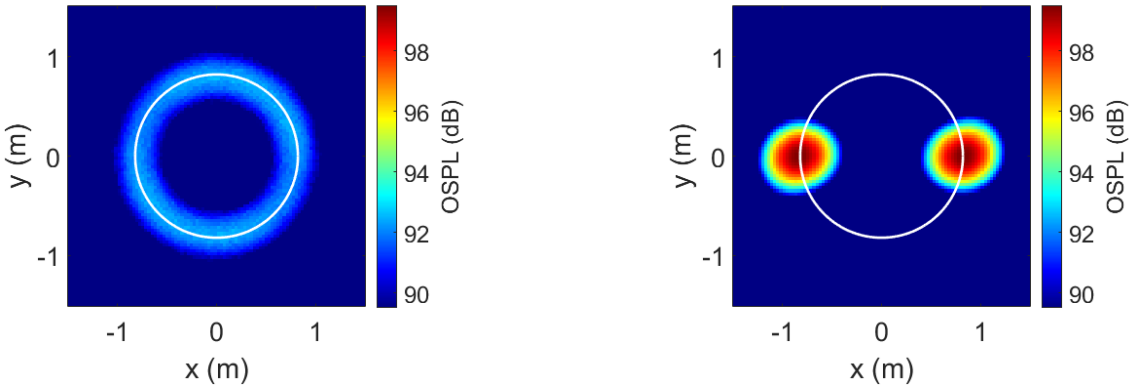

(a) CTDB *(b) ROSI*

Figure 1: Acoustic imaging methods applied to a simulation of two rotating sources. The sources rotate counterclockwise at 2010 RPM and each have an OSPL of 100 dB. The starting position of the sources is at (0.82,0) and (-0.82,0).

$$A(j,f) = \frac{1}{2}\frac{\mathbf{g}^*\mathbf{P}\mathbf{P}^*\mathbf{g}}{\|\mathbf{g}\|^4} \tag{3}$$

in which * denotes the complex conjugate transpose and $\mathbf{P}$ is the measured sound pressure vector consisting of the Fourier coefficients at f for all microphones. Furthermore, Eq. 3 contains the steering vector $\mathbf{g}$ which accounts for the phase delay and attenuation when the pressure wave travels from grid point j to microphone n. A component of $\mathbf{g}$ is defined as

$$g_n(j,f) = \frac{1}{r_{j,n}} e^{-2\pi i f \Delta t_{j,n}} \tag{4}$$

The source map is often constructed over a range of frequencies for which the source power from Eq. 3 is incoherently added over the frequencies. The incoherent addition dampens the effect of side and grating lobes stemming from the single frequency point spread function as their location is frequency dependent.

2.3 ROSI

The method that was applied for stationary sources as described in Section 2.1, can be adapted to find rotating sources [8, 13]. The difficulty with rotating sources is that at time sample k the source is at stationary grid location j, but for every following time sample, the source has a different position. Thus, to properly identify the source and verify its location and strength over multiple time samples in a time snapshot, the grid has to be turned along with the potential source. A visual representation of the grid rotation for several time steps is presented in Fig. 2.

The grid point locations of every time step are calculated as

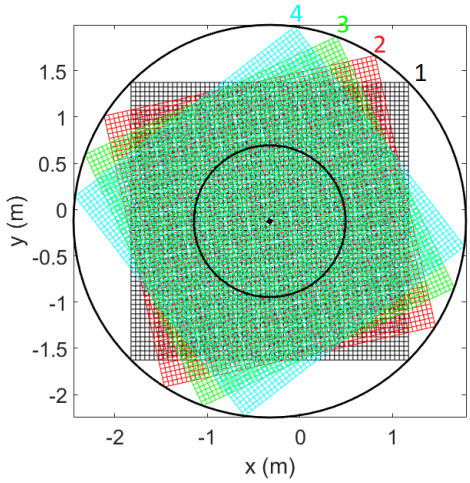

Figure 2: Example of the grid at its initial position (1) and at 50 (2), 100 (3), and 150 (4) times the sample time step later. The inner circle is the size of the propeller plane.

$$x_r(k) = x_c + R_j \cos(\psi)\cos(\Omega t(k) + \theta_j) \tag{5}$$
$$y_r(k) = y_c + R_j \sin(\Omega t(k) + \theta_j) \tag{6}$$
$$z_r(k) = z + R_j \sin(\psi)\cos(\Omega t(k) + \theta_j) \tag{7}$$

where (x_c, y_c, z) indicates the centre of rotation, ψ the grid orientation with respect to the array which is 0° for this research, and Ω the rotation speed of the source. Ω is calculated as $2\pi(\text{RPM})/60$ where RPM is the number of rotations per minute of the propeller. θ_j and R_j define the location of the grid point j with respect to the centre of the grid at the first time sample and are calculated as

$$\theta_j = \arctan\left(\frac{y_j}{x_j}\right) \tag{8}$$
$$R_j = \sqrt{x_j^2 + y_j^2} \tag{9}$$

As the grid location is different for every time sample k, the time delay also is different. $\Delta t_{j,n,k}$ is established similarly to Eq. 1 where $r_{j,n}$ now is dependent on k through the new grid locations. The emitted pressure signal from grid point j is reconstructed per sample k by selecting the received pressure at $\Delta t_{j,n,k}$. Once all samples have been considered, the reconstructed signal is further processed as described in Section 2.1. Figure 1 shows what ROSI is capable of in comparison to CTDB for rotating sources. The maximum source level is slightly below the 100 dB per source, but the source locations at the start of the rotation are correctly identified.

3 EXPERIMENTAL SETUP

The experiments for this paper were performed on a Pipistrel Velis Electro stationed at Teuge International Airport, the Netherlands. This aircraft is the first certified electric aircraft [10]. It is a two-seater aircraft with a single engine-propeller combination. The electric engine drives a three-bladed fixed-pitch propeller with a diameter of 1.64 m. It is expected that this aircraft type is a "flying propeller" as electric engines are typically silent. Additionally the impact of the airframe is expected to be low, as the landing gear is non-retractable but very thin and the airspeed is generally low.

The aircraft was parked at taxiway Charlie as this is the assigned engine run-up location at Teuge airport. There was hardly any wind, but the nose of the aircraft was turned into the little wind. An overview of the setup is visible in Fig. 3. In the figure the array is placed parallel to the propeller plane, but measurements were recorded at different positions. In total, seven positions were recorded in steps of 45° from the centre position to each side of the aircraft. No recording could be taken at the back of the aircraft, i.e. at 180°.

Figure 3: Setup engine run-up with the microphone array aligned with the propeller rotation centre.

The microphone array that is visible on the right side of Fig. 3 is a CAE Systems Bionic M-112 array [1]. It was placed 5 m in front of the aircraft nose. The system contains 112 MEMS digital microphones spread over 7 microphone arms. Additionally, a small optical camera was placed in the centre of the array. The array has been calibrated by Delft University of Technology over its acoustic frequency range through experiments in an anechoic room. The layout of the array is presented in Fig. 4.

The array has a sampling frequency of 48 kHz for the acoustic signal. For CFDB and the measured spectrum presented in Section 5.1, a block was selected of length 4096 samples, which

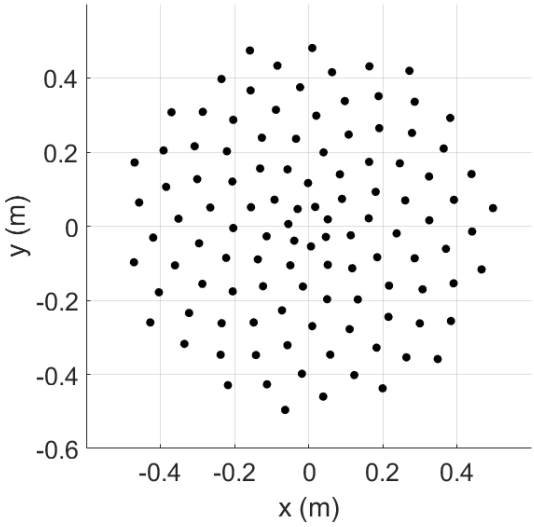

Figure 4: Microphone lay-out of the CAE Bionic M-112 array. The array's diameter is 1 m.

are Hanning weighted and consecutively zeropadded by 4096 samples. Thus, the frequency step is 5.85 Hz. For the spectrum, the signal was assumed to be ergodic and hence multiple blocks have been selected with an overlap of 50% to increase the signal-to-noise ratio.

In addition to the microphone specifics, some aircraft specifics have to be known for ROSI. These can be extracted from the cockpit dashboard of which a screenshot from GoPro footage is shown in Fig. 5. Additionally, the rotation direction of the propeller is required. For the Pipistrel Velis Electro, this is clockwise as seen from the pilot, i.e. counterclockwise as seen from the array. The propeller is rotating at 2010 RPM for the snapshot considered. This means the rotation frequency is 33.5 Hz and that the Blade Passing Frequency (BPF) is 100.5 Hz. In the time selected for the snapshot considered with ROSI, i.e. 8192 samples, the propeller rotates roughly 5.7 times.

Figure 5: GoPro photo of the cockpit instruments at the time of the measurement.

4 PROPELLER NOISE CHARACTERISTICS

To aid the understanding of the results presented in Section 5, a brief introduction into propeller noise is given. Propeller noise is dominated by tones that occur at the BPF and its harmonics [5, 11]. These tones are a result of the periodic propeller motion, as the rotation of the blades excites a volume of air in the propeller plane at the time of blade passing. The passing blade has two effects on the surrounding volume of air: (1) thickness noise, a monopole source, due to the displacement of the air volume by the passing blade volume, (2) loading noise, a dipole source perpendicular to the blade, as a result of the pressure field on the blade causing a pressure field in the surrounding air volume. The thickness noise is dependent on the local velocity. At the blade tips, the relative velocity of a blade section is higher and thus the thickness source is stronger than for blade sections closer to the propeller hub.

Throughout a rotation these effects are expected to be the same at every blade position, and therefore thought of as steady. However, often the blade loading is unsteady due to a non-uniform inflow or recirculation of flow around the propeller which is especially the case in this stationary setup. The variations in loading cause harmonics of the BPF. Note that other tonal sources may be present as well that are not subject to the BPF. These sources can for example be due to a cavity on the blade.

Additionally, there is broadband noise present in the spectrum, albeit lower than the tonal contribution for low Mach numbers. The broadband noise is caused by turbulent flow over the blades. These sources are quadrupole sources, but exhibit a dipole-like directionality close to a surface [3]. They propagate less effective to the far-field.

It is important to realise that the thickness and loading tonal contributions are not present on a blade itself. The blade merely causes them as it excites a volume of air by a blade passing in the propeller rotation field. Yet, the turbulent trailing edge noise is a source of the blade. As a measurement is performed at a distance, looking at the propeller plane and not on the propeller itself, it is expected that loading and thickness noise as well as sources on the blade occur in the measured pressure field. ROSI finds rotating sources, thus definitely finds the sources on the blade such as the turbulent trailing edge noise or a cavity on the blade. However, we expect that ROSI will also find sources that are excited at the rotational speed. From a distance, these sources look as if they are moving along with the blade and hence we expect ROSI to also find the thickness and loading noise contributions.

5 RESULTS AND DISCUSSION

In this section, a general assessment of all measurements is presented in Section 5.1. Following that, a more in-depth analysis of a selected measurement was performed and can be found in Section 5.2.

5.1 Basic assessment of measurements

Before the acoustic imaging methods were applied to the data, a more general analysis of the whole campaign was performed. Although currently only the measurements at 0° were analysed with acoustic imaging methods, the other angles will be analysed in later stages.

First, the OSPL is calculated at every measurement position. This is normalised with respect to the 0° location. Figure 6 shows the directivity from the propeller with the normalised OSPL. It is not yet clear why there is an increased OSPL on the side of the upgoing blade, but this might be due to stronger blade loading instabilities or other sources present on that side of the aircraft. Additionally, the effect of convective amplification in the measurements has to be investigated. This will be researched with acoustic imaging methods in the future.

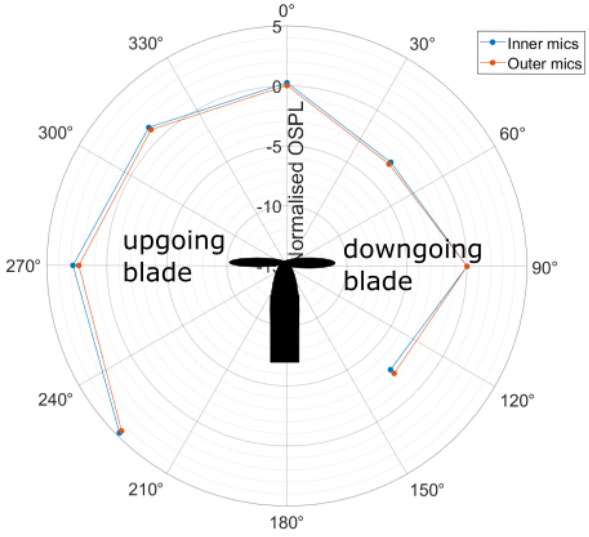

Figure 6: Directivity of the propeller where 0° is the position also displayed in Fig. 3, hence parallel to the rotation plane, and 90° and 270° are perpendicular to the rotation plane.

In addition to the OSPL at each measurement position, the spectrum was also constructed. These spectra are presented in Fig. 7. The BPF and harmonics align neatly for each position, but the respective strength of the tones varies. This might be due to different loading on the blade.

Following this short general assessment, the measurements at the 0° location are investigated. For the upcoming results, no correction for convective amplification is introduced. For the analysis of stationary sources, this effect should not play a role in general. For ROSI in this setup, where the array plane is parallel to the propeller plane, it is expected that the amplification averages out over multiple rotations and over the microphone locations. The atmospheric absorption is neglected as in the 10 to 10,000 Hz band at a 5 m distance it is only 0.73 dB for 10,000 Hz and lower for the frequencies below 10,000 Hz.

5.2 Acoustic imaging results

The acoustic imaging methods were applied to the data to identify all noise sources and interaction effects. First, CTDB and ROSI were applied over the full frequency range. The results of this are presented in Fig. 8. Note the significant difference in the OSPL levels. The maximum in ROSI is below the scale in CTDB. The CTDB result shows a dominating source on the lower right side, at the ground, where the propeller is moving upward. From this image it is not clear

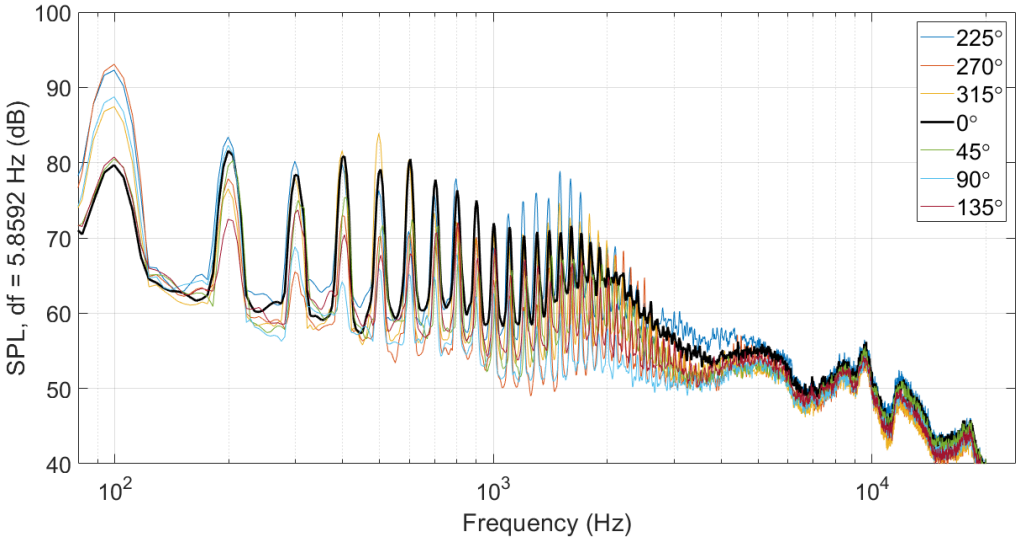

Figure 7: Spectrum of a single centred microphone for the engine run-up at all angles. Levels at source location.

whether this source is an effect of a stationary algorithm fitting a moving source, or that it is truly a source. It is for example possible that at this location the wake of the propeller interacts with the nose landing gear wheel.

The ROSI result shows one large mainlobe with peaks in three directions. These peaks indicate the starting position of the blades for the selected time snapshot. The reason that the blades cannot be identified separately, is that the spatial resolution is not sufficient. The blade tips are 1.42 m apart because the angle between the blades is 120 deg and the radius of the blade is 0.82 m. Thus the minimum frequency at which the blades are separately visible in a beamform map is 1.5 kHz. The spatial resolution has a large impact on the ROSI maps as the lower frequencies are strongest as can be seen in Fig. 7. Thus, these levels dominate the overall source map.

To assess the blade locations and the performance of ROSI, the time-domain data is bandpassed from 1.5 to 10 kHz for three different snapshots in the recorded time signal. Figure 9 shows that at this frequency range the individual blades are visible. Additionally, by looking at the maximum level for each map, it becomes clear that the level of the rotational sources varies slightly over time, which might be due to inflow conditions. Per time step of 0.3 s the blades are expected to turn 10.05 rotations. Thus, 10 full rotations and 20° extra which roughly agrees with the results when looking at the dominant blade between 3.3 and 3.6 s. For 3.9 s it is not as clearly visible as another blade seems dominant.

A few interesting frequency bands have been further analysed. Figure 10 presents incoherently summed CFDB results and ROSI results with a bandpass filter on the time-domain signal for three frequency ranges. The methods can be compared side by side for difference in source velocity domain or top to bottom for differences in spatial and frequency domain. Note that all the maximum levels have been added in the caption for each figure in Fig. 10 for easy comparison. The dynamic range for all images equals 3 dB.

What stands out from the CFDB results is that the lower right source is dominating the beam-

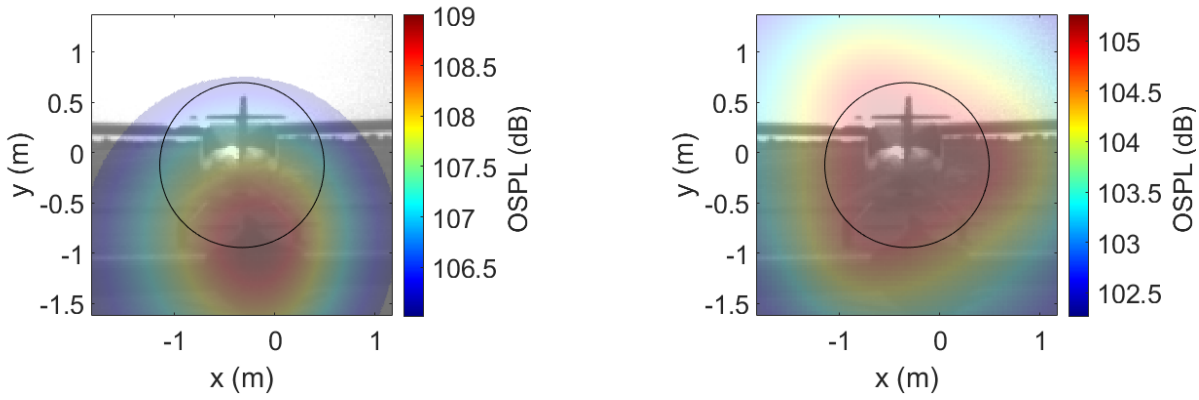

(a) CTDB *(b) ROSI*

Figure 8: CB and ROSI applied to the full time-domain signal. Note the significant difference in OSPL on the colour axis.

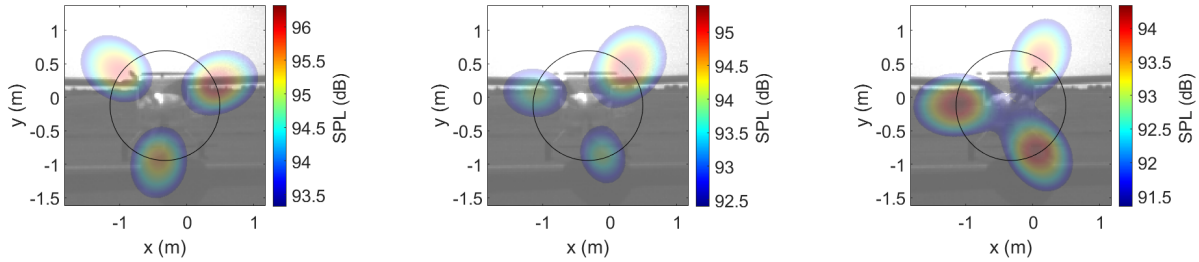

(a) t = 3.3 s, SPL_{max} = 96.3 dB *(b) t = 3.6 s, SPL_{max} = 95.7 dB* *(c) t = 3.9 s, SPL_{max} = 94.3 dB*

Figure 9: ROSI on different time snapshots. The bandwidth for all three source map is 1.5 to 10 kHz. The colourbar represents the total level over the selected frequency band and has a dynamic range of 3 dB for all three images.

form levels. From the simulation in Fig. 1 it was expected that a ring of increased levels would be present, but this only happens for higher frequency ranges where the source strength of the blades increases relative to the source strength of the stationary source from Fig. 10a. Additionally, the ground reflection of the stationary source is visible. As stated before, it is not yet clear what is causing this source. This can be investigated further by applying imaging to different measurement angles, such as the right side view angle. Also by varying the distance of the scan plane to the array, perhaps the source location can become more present.

When considering the acoustic imaging results of ROSI, it is important to observe the levels in the source map. First a comparison with the CFDB images is made. For the lower two frequency ranges, the stationary source has a higher maximum level but for the highest frequency range (Figs. 10e and 10f) the rotating sources are stronger. When comparing all ROSI images for the different frequency bands, it becomes clear that a blade can be stronger or weaker than the others at different frequency ranges. For example, the rightmost blade is the strongest for 6.1 to 6.6 kHz, but this is not true for 2.1 to 2.6 kHz. On these large frequency ranges, no other sources than the propeller blade tip show up. Hence, it is assumed for now that no cavity or

blade impurity is present. Furthermore, it is important to note that the stationary source is not visible in the ROSI images thus proving the ability to separate sources in the velocity domain by applying both imaging methods.

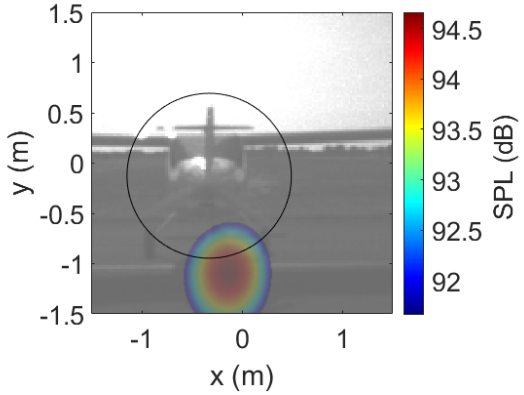

(a) CFDB 2.1 to 2.6 kHz, SPL_{max} = 94.7 dB

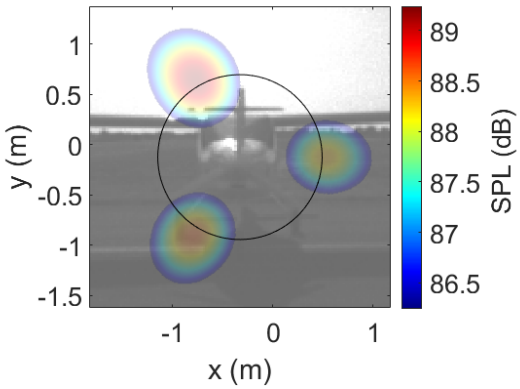

(b) ROSI 2.1 to 2.6 kHz, SPL_{max} = 89.3 dB

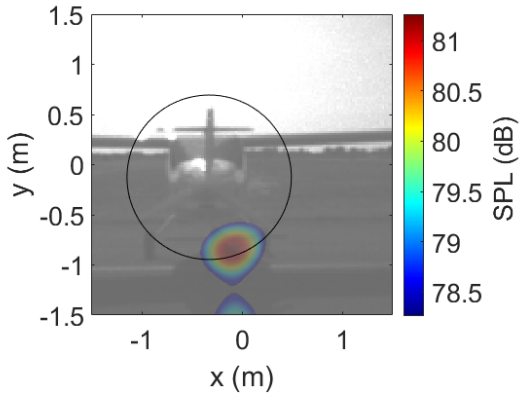

(c) CFDB 3.6 to 4.1 kHz, SPL_{max} = 81.2 dB

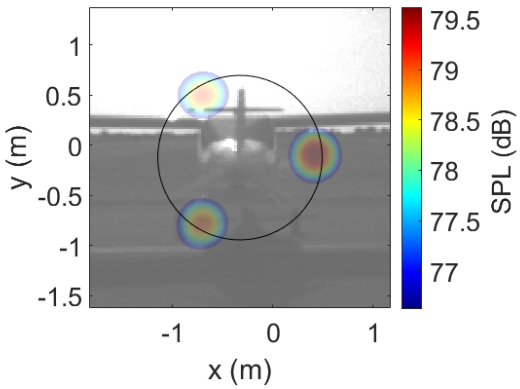

(d) ROSI 3.6 to 4.1 kHz, SPL_{max} = 79.6 dB

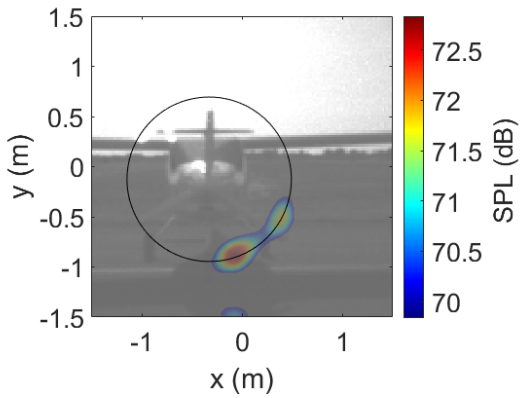

(e) CFDB 6.1 to 6.6 kHz, SPL_{max} = 72.8 dB

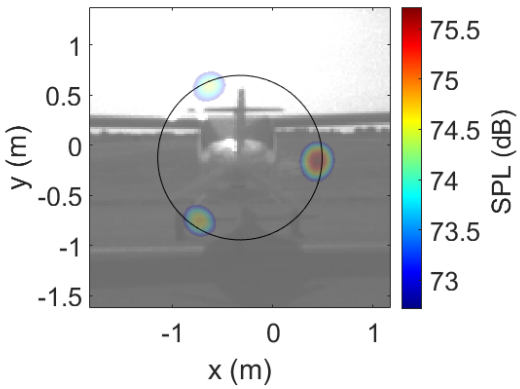

(f) ROSI 6.1 to 6.6 kHz, SPL_{max} = 75.8 dB

Figure 10: Comparing CFDB and bandpass filtered ROSI on different frequency ranges. The colourbar represents the total level over the selected frequency band. The colourbar has a dynamic range of 3 dB for all images.

6 CONCLUSIONS

This research covered the first steps towards understanding the sources present in full-scale propeller noise measurements and how to identify them. This understanding is necessary for the validation of propeller noise prediction models on full-scale measurements as it aids in separating the propeller from the stationary sources. From this initial research, the strength of using ROSI already became apparent. The three blades can clearly be separated at higher frequencies. The next step in this research is to investigate the spectrum decomposition of the measured signal into stationary and rotating sources. After that, this spectrum separation should be performed at every measurement angle to identify sources that are not directly in the propeller plane. This might also give more insight into the directionality of the sources.

Ultimately, this method should be applied to fly-over measurements of propeller aircraft as it will provide the most accurate validation data for propeller noise prediction models. The propeller then operates in free stream inflow and recirculation effects and unsteady blade loading will be reduced. This however requires the addition of forward velocity terms in ROSI to account for the helical propeller movement.

7 ACKNOWLEDGEMENTS

The authors would like to thank several parties for their contribution in the measurement campaign. E-flight Academy provided the pilot and Pipistrel Velis. The technical team of the TU Delft-NLR co-owned Cessna Citation II provided technical support and safety supervision on the airside. International Airport Teuge aided in making the measurements safe and possible on their airport. The authors would like to thank Dutch Electric Aviation Centre (DEAC) Teuge for their financial contribution to the operational cost of the aircraft during the measurement campaign.

REFERENCES

[1] CAE Software & Systems. "Acoustic Camera 112 Microphones." URL `https://www.cae-systems.de/en/products/acoustic-camera-sound-source-localization/bionic-m-112.html`, Last visited: 1 May 2022.

[2] Civil Aviation Authority. "Emerging Aircraft Technologies and their potential noise impacts." Technical Report CAP 1766, 2019.

[3] N. Curle. "The influence of solid boundaries upon aerodynamic sound." *Proceedings of the Royal Society of London. Series A. Mathematical and Physical Sciences*, 231(1187), 505–514, 1955. ISSN 0080-4630. doi:10.1098/RSPA.1955.0191.

[4] D. L. Huff, B. S. Henderson, and E. Envia. "Motor Noise for Electric Powered Aircraft." In *22nd AIAA/CEAS Aeroacoustics Conference*, pages 1–12. Lyon, France, 2016. doi: 10.2514/6.2016-2882.

[5] J. E. Marte and D. W. Kurtz. "Review of Aerodynamic Noise From Propellers, Rotors, and Lift Fans." Technical Report 31-1462, NASA, 1970.

[6] D. A. I. Mccurdy, C. A. I. Powell, and N. I. Si. "Annoyance Caused By Propeller Airplane Flyover Noise : Preliminary Results." *Nasa Technical Memorandum*, 1981.

[7] R. Merino-Martínez. "Microphone arrays for imaging of aerospace noise sources." 2018. doi:10.4233/uuid. PhD thesis, Delft University of Technology.

[8] S. Oerlemans, P. Sijtsma, and B. Méndez López. "Location and quantification of noise sources on a wind turbine." *Journal of Sound and Vibration*, 299(4-5), 869–883, 2007. ISSN 0022-460X. doi:10.1016/J.JSV.2006.07.032.

[9] M. Y. Pereda Albarrán, M. Kreimeier, W. Enders, and E. Stumpf. "Noise evaluation of battery powered small aircraft." *CEAS Aeronautical Journal*, 11(1), 125–135, 2020. ISSN 18695590. doi:10.1007/S13272-019-00404-2.

[10] Pipistrel Aircraft. "Velis Electro EASA TC." URL `https://www.pipistrel-aircraft.com/aircraft/electric-flight/velis-electro-easa-tc/#tab-id-1`, Last visited: 1 May 2022.

[11] R. H. Self. "Propeller Noise." *Encyclopedia of Aerospace Engineering*, 2010. doi:10.1002/9780470686652.eae339.

[12] P. Sijtsma. "Beamforming on moving sources." Technical Report NLR-TP-2006-733, Netherlands Aerospace Centre, 2007.

[13] P. Sijtsma, S. Oerlemans, and H. Holthusen. "Location of Rotating Sources by Phased Array Measurements." In *AIAA/CEAS Aeroacoustics Conference*. Maastricht, Netherlands, 2001. ISSN 2001-2167. doi:10.2514/6.2001-2167.